Diffracted Beams from Metasurfaces: High Chiral Detectivity by Photothermal Deflection Technique

Grigore Leahu,* Emilija Petronijevic, Roberto Li Voti,* Alessandro Belardini, Tiziana Cesca, Giovanni Mattei, and Concita Sibilia

Measurements of difference in optical interactions between circularly polarized excitations of opposite handedness (circular dichroism) are highly important for both natural and artificial chiral structures. Here the photothermal deflection technique is proposed as a method to detect the optical chirality of a metasurface, analyzing the diffracted beams by the metasurface itself. Two metasurfaces are investigated, based on Au and Ag. The samples are fabricated by nanosphere lithography, with a tilted deposition of thin metal layer, which produces symmetry-breaking. The unit cell periodicity of these metasurfaces allows for multiple order diffraction in the 450–520 nm range, which encompasses the emission lines of an Ar laser. The metasurfaces are placed on a mirror and excited by an Ar pump beam at different orientations, laser wavelengths, and circular polarization degree; the probe beam scans the absorption of the diffraction orders back-reflected from the underlying mirror. In this way, the chiral investigation is simplified by placing the scanning of absorption-induced thermal effect into the metasurface plane, thus avoiding the transmission/reflection measurements of a specific order, which are done by angular placement of detector. Theoretical and numerical approaches are further developed to reconstruct both thermal and optical behavior of the chirality at the nanoscale.

1. Introduction

Chirality, a lack of the mirror symmetry of an object, is a common property of our world, present in DNA, sugars, amino acids, drugs and so on. Being "left" or "right" at a molecular level can influence biological activity and toxicity;[1,2] these two versions of the same molecule are called enantiomers, and while one enantiomer acts as a drug, another one can be inactive or even lead to serious side-effects.[3] Therefore, there is a growing need for ultrasensitive chiral detectors. In absorbing materials, chirality is probed by measuring the difference in the absorption between left and right circular polarization (LCP and RCP, respectively); this difference is defined as circular dichroism (CD). However, natural CD of chiral molecules is usually extremely low and lies in the ultraviolet wavelength range, which makes conventional CD techniques bulky and insensitive to low enantiomeric concentrations.

Over the past years, there has been a wide interest in enhancing the enantioselectivity by means of specially designed nanostructured materials. Specifically, plasmonic nanostructures with chiral shapes have been proposed for the enhancement of chiral matter–light interaction. Highly sophisticated fabrication techniques have led to the development of gammadion-like or helix-shaped nanoresonators, periodically organized to form a metasurface; the overall response of such nanostructure does not possess mirror symmetry and exhibits CD response at normal incidence.[4–8] While these so-called intrinsic chiral structures usually require costly and time-consuming nanofabrication, alternative approaches were proposed for the symmetry breaking at oblique incidence, i.e., to get extrinsic chirality. Such nanostructures usually contain a plasmonic layer asymmetrically deposited on an achiral substrate, and can be fabricated by means of simple, low-cost, self-assembling techniques. The extrinsic CD response is then obtained by the proper alignment of the sample's orientation and light wavevector at oblique incidence.[9–15] On the other side, employing metasurfaces with a diffractive nature at wavelengths comparable to their dimensions was shown to produce interesting chiral phenomena in higher-order diffracted beams.[16–18] Finally, achiral structures excited by LCP or RCP were proposed for near-field enhancement of enantioselectivity without the nanostructure's background signal.[19–21]

While a vast numerical work has been done to optimize nanoscale geometry for the interaction with chiral molecules, it should be noted that the experimental demonstrations of

G. Leahu, E. Petronijevic, R. Li Voti, A. Belardini, C. Sibilia
Department S.B.A.I
Sapienza Università di Roma
Via A. Scarpa 14, Rome I-00161, Italy
E-mail: grigore.leahu@uniroma1.it; roberto.livoti@uniroma1.it
T. Cesca, G. Mattei
Physics and Astronomy Department
University of Padova
Via Marzolo 8, Padova I-35131, Italy

molecule-nanostructure CD response still face challenges, and they are not exhaustive. First, there is a discrepancy in the spectral overlap between the conventionally fabricated nanostructures and short-wavelength CD spectra of molecules. This is mainly due to the fact that nowadays noble metals are typically used for the nanoresonator constituents in a unit cell of a plasmonic metamaterial. Therefore, the nanostructures' CD lies in the visible and near-infrared range. Second, conventional CD characterization techniques use the zeroth-order transmission to calculate the extinction and relate it to the energy absorbed by the material, therefore lacking a direct characterization of the scattering-free absorption signal. To this end, we proposed photoacoustic spectroscopy[22,23] as a useful characterization technique of absorptive properties in nanostructures, and we further used it with chiral excitation.[10,12] However, for a better overlap with chiral molecules' CD, a blue shift of the nanostructures' spectral range is needed; this corresponds to the additional shrinkage of nanoscale dimensions, which ultimately complicates the nanofabrication.

This work proposes the photothermal deflection technique to study chirality in diffractive metasurfaces; such characterization is highly sensitive, scattering-free, nondestructive, and offers simplicity with respect to the diffraction spectroscopy. We investigate two Ag- or Au-functionalized metasurfaces fabricated by a low-cost self-assembling technique; the periodicity of both metasurfaces is 522 nm, which gives diffractive orders in the blue-green part of the spectrum. We monitor chiral response at four wavelengths of an Ar pump beam, which is diffracted by the metasurface and back-reflected by an underlying mirror; this way local absorption is measured by means of a deflected He–Ne laser beam, thanks to the "mirage effect". We investigate how the chirality is dependent on the wavelength, on the order's spatial position, and on the incident angle of the Ar beam. The estimate of the temperature rise and thermal gradients produced by the diffracted beams is eventually reconstructed by experimental results. We believe that this novel approach, based on thermal consequences of chirooptical phenomena, can be generally used for chirality measurements in metasurfaces, thus being of importance for chiral sensing applications.

2. Photothermal Deflection Technique

The photothermal deflection technique (PDT) offers a nondestructive and scattering-free approach with high sensitivity with respect to the conventional non-thermal methods (transmission or reflection spectroscopy). It was applied to study absorption properties of organic thin films,[24] opals,[25] III–V semiconductors and alloys[26,27] etc. More recently, it has inspired novel techniques for characterization of highly luminescent materials; in ref. [28] it was applied in photothermal threshold quantum yield measurements of CdSe/CdS quantum dots, while in ref. [29] it was combined with a Sagnac interferometer to study the photothermal excitation spectrum of a highly luminescent phosphor. Finally, although PDT was applied to study plasmon-enhanced Si thin films for solar cell applications,[30] it has never been applied to study plasmonic metasurfaces and their chiral properties.
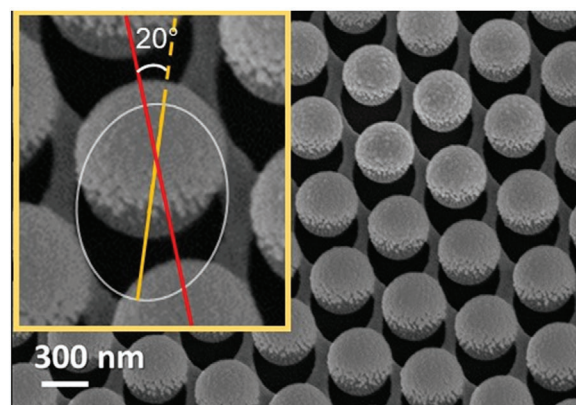

Figure 1. Scanning electron microscopy images of samples Ag-SNSA, insert in-plane tilt angle of 20° of the Ag flux direction (red line—the axis of the hexagon, yellow line—Ag flow direction, white ellipse—elliptic nanohole due to the shadowing effect).

In this work, we apply the PDT to study chirality of diffractive metal-polystyrene metasurfaces. The plasmonic semi-nanoshell arrays (SNSAs) are fabricated by nanosphere lithography with inclined metallic depositions, in a multi-step process.[12,31] First, a self-assembled monolayer of polystyrene (PS) nanospheres (MicroParticles GmbH, Germany) of diameter 522 nm is formed on "piranha" cleaned soda-lime glass substrates, in order to obtain a hexagonal ordered array. Then the diameter of the PS nanospheres is reduced down to $D = 370$ nm, preserving the ordered arrangement, by a reactive ion etching (RIE) process performed in an $Ar-O_2$ atmosphere (30% Ar – 70% O_2) at a power of 15 W for 10 min. Subsequently, a thin metallic layer (50 nm thick) of Ag or Au is thermally evaporated on the nanospheres at an inclination of 45° with respect to the sample's surface. The thickness of the metallic layer is evaluated during the thermal evaporation by using a calibrated quartz microbalance. For the Ag-SNSA sample, an in-plane tilt angle of 20° of the Ag flux direction is introduced during the thermal evaporation.[12] **Figure 1** shows the FE-SEM image, in plane-view, of the sample Ag-SNSA. In Figure S1 (Supporting Information), we show the FE-SEM image of the sample Au-SNSA, the fabrication of which did not include the in-plane tilt.

Transverse photothermal deflection methods are based on the use of two laser beams, orthogonal to each other, one for heating the sample (pump) and the other (probe) to detect, through the beam deflection effect, the produced temperature gradients in a deflection medium.[32,33] In the transverse standard scheme[34,35] the probe laser beam travels in air skimming the sample surface heated by the pump beam whose intensity is periodically modulated. In this configuration different methods have been tested and applied to measure the thermal diffusivity of various solid materials in the range between 10^{-3} to 20 cm^2 s^{-1}. For samples of relatively large geometric dimensions (larger than the Rayleigh distance), the bouncing method is used, and the direction of the probe beam is inclined with respect to the sample surface by a small angle (typically few degrees) and the beam "bounces" on the sample surface[36] close to the heating zone. Theory of photothermal deflection in transverse configuration states that the probe beam is deflected from its original trajectory due to the air thermal gradient produced by the heat

**ADVANCED
SCIENCE NEWS**
www.advancedsciencenews.com

**ADVANCED
OPTICAL
MATERIALS**
www.advopticalmat.de

source (mirage effect). The lateral deflection angle Φ_y is accumulated along the probe beam path, and eventually detected by a position-sensitive photodiode. The quantity Φ_y is given by the well-known expression:[35,36]

$$\Phi_y = \frac{1}{n}\frac{dn}{dT}\int_x \frac{dT}{dy}\,dx \tag{1}$$

where in air the refractive index is $n \approx 1$, while the optothermal coefficient is $dn/dT \approx -10^{-6}$ K^{-1}. The important feature of PDT that distinguishes it from other photothermal techniques (from photoacoustics in particular) is the 1D spatial resolution along the pump-probe scan line. This feature is the basis of the new application of the PDT that we propose in this article for the study of the chiral properties of diffracted light beams.

Figure 2a represents the optomechanical part of the set-up for the measurement of the photothermal deflection signal in bouncing configuration. An Ar laser (Coherent Innova 70), periodically modulated in intensity by a mechanical chopper, is used as a pump beam. A He–Ne laser (Spectra Physics) is used as a probe beam. The pump beam (spot size 70 μm) impinges in the y-z plane, and excites the sample, while the probe beam (spot size 35 μm) propagates along the x direction and, after reflection at a glazing angle on the sample surface, it ends up on the 2D position sensor (SiTek 2L10, active area 10 × 10 mm^2). The output of the position sensor is connected to the input of a vector lock-in (EG&G Instruments 7260), which measures both amplitude and phase of the deflection signal. Motorized translation stage, PC-controlled, allows to vary the pump-probe distance in the y direction (y scan) to measure the spatial distribution of the photothermal deflection signal on the metasurface. Figure 2b shows the real image of the diffracted orders in Ag-SNSA metasurface transmitted through the glass substrate and reflected back toward the metasurface from the mirror under the sample when it is excited by a pump beam at 458 nm. The light of the diffracted modes is partially absorbed in the SNSA metasurface, creating heat sources. Note that absorption sensitivity of PDT in solids is very high, of the order of 10^{-7} cm^{-1}. As it can be seen from the photograph, the six diffracted orders are placed at the vertices of a regular hexagon, while the incident pump beam creates the heat source in its center. Figure 2c shows the geometric sketch of the angular position of the symmetry axis of the hexagon with respect to the propagation direction x of the He–Ne laser beam and the direction of the scan y. The position of each heat source center is identified by the condition $\Phi_y = 0$. The mode numbering from −3 to +3 corresponds to the scan sequence of each of them as found along with the scan (see also the photo in Figure 2b). Figure 2c clarifies that by measuring the deflection signal versus the pump-probe distance, the positions of the modes are projected on the line that passes through the center of the hexagon (the point of incidence of the pump beam) and coincides with the scan direction y. One way to detect the presence of all the seven heat sources (incident and six diffracted beams) at the same time in one measurement can be obtained by choosing the probe beam path with a misalignment angle α with respect to the symmetry line of the hexagonal diffraction pattern, and by varying the pump-probe distance from −2.5 to +2.5 mm, as it will be discussed later.
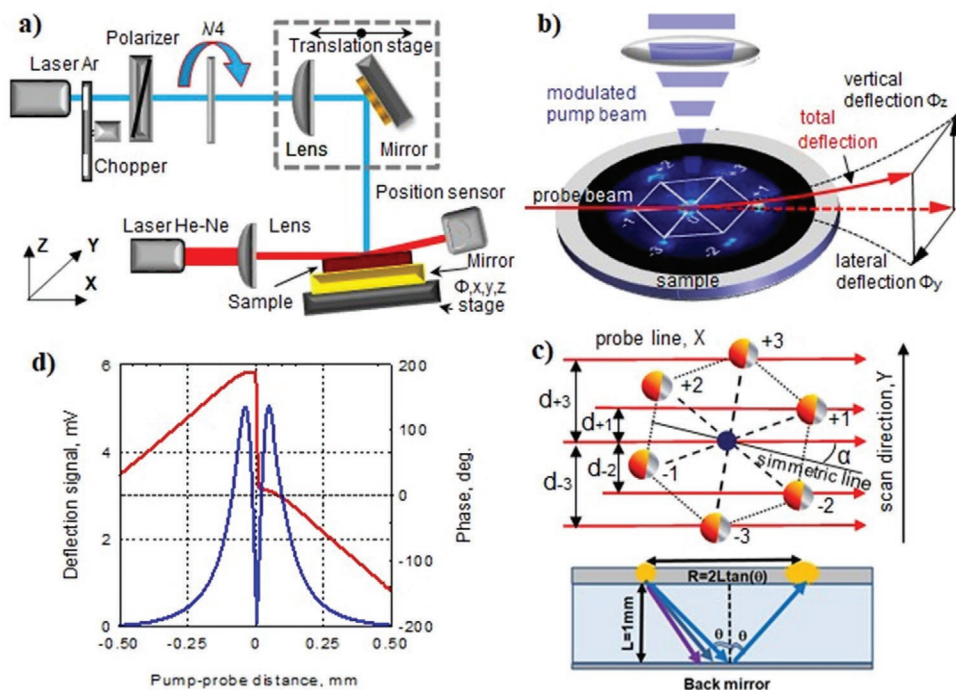

Figure 2. a) Optomechanical part of the set-up for the measurement of the photothermal deflection signal. b) Photograph of the six diffracted orders in Ag-SNSA metasurface when it is excited by a pump beam at 458 nm, and schematic view of the two components of the deflection angle of the probe beam. c) Geometric view of the position of the hexagon formed by the diffraction modes with respect to the propagation direction x of the He–Ne laser beam and the direction of the scan y, the misalignment angle α is shown. d) Example of amplitude (blue line) and phase (red line) of the deflected signal at 9 Hz as a function of pump-probe distance measured for a thin layer of Ag on glass substrate.
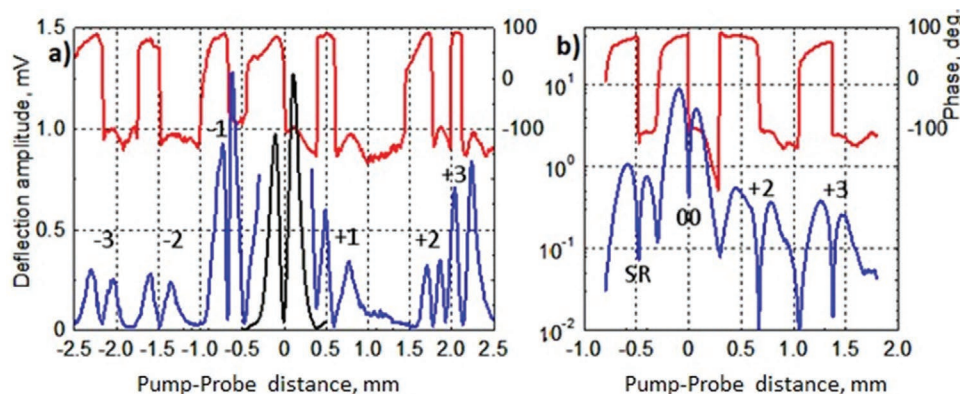
2100670 (3 of 11)

ADVANCED
SCIENCE NEWS
www.advancedsciencenews.com

ADVANCED
OPTICAL
MATERIALS
www.advopticalmat.de

Figure 3. Amplitude (blue and black curve) and phase (red curve) of the PD signal for Ag-SNS excited with the Ar beam at 514 nm modulated at 36 Hz, displayed as a function of the pump-probe distance. The numbers on the curves indicate the position of the diffraction modes. a) Results for sample Ag-SNSA excited at normal incidence. The black curve is the signal coming directly from the point of incidence of the pump beam and was decreased by 15 times to improve observation. b) Results for sample Ag-SNSA excited at 20° incidence along the Ag flux direction. SR is the specular reflection (not diffracted), 00 is the point of incidence of the pump beam, while the numbers +2 and +3 indicate two observed diffraction modes.

As an example, Figure 2d shows the amplitude and phase of the lateral deflection signal as a function of the pump-probe distance, measured at 514 nm for a homogeneous thin layer of Au on glass substrate (in the unpatterned part of Au-SNSA). Furthermore, the spot size of the pump beam can be estimated from the distance between the two maxima of the deflection amplitude. Just in the middle of the two maxima there is a position where no lateral deflection is observed corresponding to center of the heat source produced by the diffracted orders. For this reason, the lateral component of the deflection signal is used to measure precisely the beam center. As it can be seen from Figure 2d, at the position that corresponds to zero of the signal amplitude, the phase (red line) is subjected to a prompt variation of 180 degrees due to the change in the direction of deflection from left to right.

Next, we present the experimental results when the sample is excited with the Ar beam at 514 nm and at 36 Hz modulation frequency. In **Figure 3**a, the pump beam excites Ag-SNSA under normal incidence. We observe seven signal sources: the central one corresponds to the pump beam, while the other six sources are symmetrically distributed with respect to the zero position, on the left −3, −2, −1, and on the right +1, +2, +3, as defined in Figure 2b,c. The central signal (black curve) generated directly by the absorption of the pump beam by the sample at the incident point is more than an order of magnitude larger than the signals from the diffracted beams, and has been attenuated of 15 times to improve observation. Amplitude (in log scale) and phase of the PD signal for sample Ag-SNSA excited at 20° of incidence along the Ag flux direction are presented in Figure 3b. In Figure 3 it can be seen that in the centers of the heat sources, where the signal amplitude is minimum, the phase shifts from +90° at −90°. The experimental values of the PD signal phase will be used for thermal profile reconstruction in Section 4.3.

3. Numerical Optical Reconstruction

We previously used a commercial 3D finite difference time domain (FDTD) solver in Lumerical[37] to model the experimental data and gain detailed insight into the electromagnetic behavior

in such metasurfaces.[12,38,39] Specifically, we modeled total absorption and zeroth-order transmission. Here, instead, we adapt Lumerical to investigate near-to-far field transformation of the chirality in the metasurfaces. In **Figure 4**a,b, we show a schematic of the simulation set-up (see Experimental section for the simulation set-up details). The metasurface is excited from the airside; the plane of incidence can be in the xz- or yz-plane, depending on the experimental configuration. The near-field monitor just below the metasurface ($z = −50$ nm) decomposes the total transmitted field into diffracted orders (Figure 4a) and projects them to the far-field. An example of a single simulation result is given in Figure 4b, for the Ag-SNSA excited at 20° by a LCP wave of 514 nm. In this scenario, the incident light is impinging from the right side (pink circle) in the xz-plane, at 20° of incidence with respect to the normal to the sample's surface, which is given by vector $\vec{s}$. The result is the far-field intensity of the specular order (denoted as (0,0)), and six other orders, as well as their angular position in the far-field plane, given by an angle θ_{ff}. It should be noted that this technique considers the far-field projection to a homogeneous soda-lime glass medium; however, since these fields are back-reflected by a perfect mirror, they can be considered to exist at the sample's surface at a distance of $2L\tan(\theta_{ff})$ from the center (L is the thickness of the soda-lime substrate, see Figure 2c). The far-field center corresponds to the position of the central, pump-generated heat source in the experiment. Therefore, the intensity of the orders can be correlated to photothermal deflection.

The following reconstruction demonstrates why the intensities of the diffracted orders differ for LCP and RCP, exhibiting extrinsic chirality. We use various excitation schemes, with LCP (blue) or RCP (red) light at 488 nm. We export the diffracted orders to a 3D figure, where the positions of the orders are given by the hexagon from Figure 4b, while the peaks of the Gaussian functions are given by the extracted intensities of the orders. The specular order (0,0) carries substantially higher intensity (Figure 4b), which is not of interest in the PDT, because its light is overwhelmed by the pump beam; therefore, here we omit it for the sake of clarity. We first simulate a version of the Ag-SNSA, where PSN were symmetrically covered
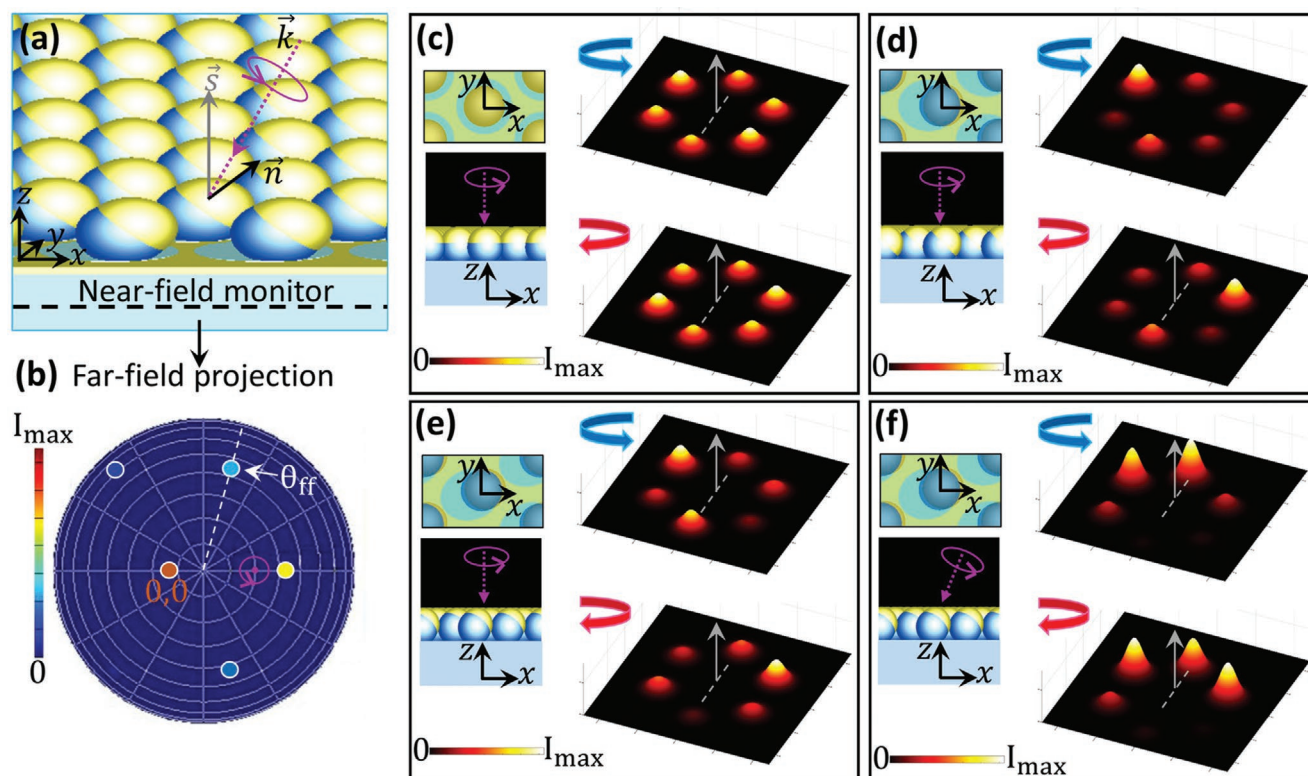
**ADVANCED
SCIENCE NEWS**

www.advancedsciencenews.com

**ADVANCED
OPTICAL
MATERIALS**

www.advopticalmat.de

Figure 4. a) Sketch of the simulation set-up: complex electromagnetic fields are caught by a near-field 2D monitor under the metasurface, and projected to the far-field hemisphere of the glass medium. b) Example of the simulation result when the Ag-SNSA is excited by an LCP wave at 514 nm, at 20° of incidence in the *xz* plane (colored circles are guide for the eye for the far-field points of the order diffraction). c) Symmetric version of Ag-SNSA (inset), when excited at normal incidence, gives orders of almost equal intensities for LCP and RCP. d) Asymmetric Ag-SNSA, made with a 45° tilted deposition in the *xz*-plane: when excited at normal incidence it gives orders of different intensities; however, for LCP and RCP excitation, these intensities are antisymmetric with respect to *x*-axis, so that the overall chirality of the metasurface is zero. e) Asymmetric Ag-SNSA, made with a 45° tilted deposition out of the *xz*-plane, introducing a 20° in-plane tilt as in Figure 1: when excited at normal incidence it gives orders of different intensities that are not anti-symmetric with respect to *x*-axis, therefore, such metasurface is intrinsically chiral. f) Same metasurface as in e), excited at 20°: it gives chirality in all the orders.

by Ag (Figure 4c) and excited at normal incidence and 488 nm. Such metasurface is made of a symmetric Ag shell on the top of the PSN, and a circular nanohole due to the shadow (inset of Figure 4c); details of fabrication of such samples can be found in ref. [12]. This metasurface is completely symmetric, and produces regular hexagonal diffraction pattern, equal for LCP and RCP excitation. Instead, in Figure 4d we consider a PSN metasurface on which the plasmonic layer was deposited at 45° in the *xz*-plane; such a tilted deposition results in an asymmetric plasmonic shell, as in our samples, and in an elliptical nanohole array on the bottom.[38,39] In this case, the diffraction orders differ in intensity for LCP and RCP excitation; however, they are antisymmetric with respect to the x-axis. When the sum of all the orders is considered, this antisymmetry leads to the vanishing absorption CD at normal incidence. It is interesting to note that we previously investigated such behavior by means of the photo-acoustic technique;[12] since this technique gives the total absorption, it gave null CD at normal incidence in Au-SNSA and Cr-SNSA. However, with PDT it is possible to access the chirality of single orders, as shown later in the manuscript.

In Figure 4e, we further consider a geometry that corresponds to the experimentally investigated sample (Figure 1), which is chiral even at normal incidence. This occurs when, along with the 45° tilted metal deposition, there is an additional in-plane tilt which breaks the in-plane hexagonal symmetry (Figure 1, and the inset of Figure 4e). Again, order intensities differ for LCP and RCP excitation, but they are no more antisymmetric with respect to the x-axis. When summed, these orders give CD even at normal incidence, which we previously measured by means of the photoacoustic technique for Ag-SNSA.[12] Finally, in Figure 4f we investigate this same geometry, but with oblique excitation, at 20° in the *xz*-plane, as it will be further considered in the experiment; we chose this angle as it previously provided the maximum absorption CD, detected by photoacoustic technique. The positions of the hexagon now shift, bringing some orders close to the excitation center. The chirality is present in all orders; some orders are twice as intense compared to previous cases, while some orders almost vanish.

4. Results and Discussion

4.1. Normal Incidence of the Pump Laser Beam

Figure 5a shows the amplitudes of the PD signal for Ag-SNSA sample when excited at normal incidence, as a function of the
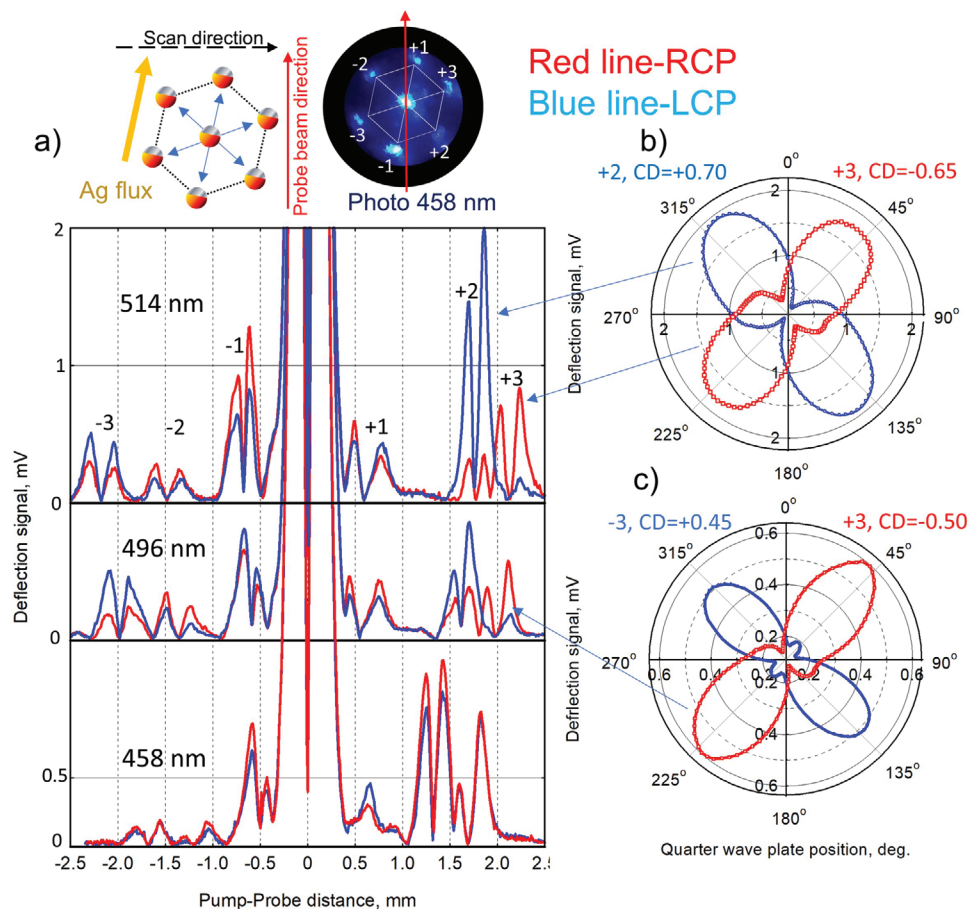
Figure 5. a) PD signal for the Ag-SNSA sample excited at normal incidence, at three pump beam wavelengths, as a function of the pump-probe distance. PD signals are displayed for LCP and RCP, in blue and red color, respectively. The signals for different wavelengths are shifted to avoid overlaps. b) Polar plots of the signals as a function of quarter-wave plate rotation for diffracted orders +2 and +3 (amplitude is magnified three times) at 514 nm, and c) for orders −3 and +3 at 496 nm.

pump-probe distance. We investigate three wavelengths of the Ar laser for LCP (the blue curves) and for RCP (the red curves). The signals for different wavelengths are shifted for the sake of clarity. In the inset of Figure 5a, we show a sketch of the scan direction, and a photograph is taken during the PD measurement at 458 nm; the six diffraction modes are placed at the vertices of the regular hexagon.

As one may see, LCP and RCP excitations give strongly different values of the PD signal, showing that PD experiment provides relevant information regarding chiral properties of diffracted orders. The position of the diffraction orders moves away from the central position by increasing the pump beam wavelength. This is in good agreement with the theory of the 2D diffraction grating, which predicts a wavelength-dependent internal angle $\theta(\lambda) = \arcsin\left(\frac{1}{n}\frac{2}{\sqrt{3}}\frac{\lambda}{a}\right)$, with $n = 1.5$ being the soda-lime refractive index, and $a = 522$ nm the periodicity (see Figure 2c). Once θ is known, the distance R of each heat source from the center can be calculated as $R = 2L\tan\theta$, and the position of the deflection zeros along the y-scan is eventually obtained by simple geometrical considerations as $d_Y = R\cos(\beta_m + \alpha)$, with α being the misalignment angle (see Figure 2c) calculated

from the experimental data, and $\beta_m = m\pi/3$ being the position angle of the m-th hexagonal vertex. From simple geometrical considerations, taken from Figure 2c, the misalignment angle can be calculated as $\alpha = \arctan\left(\frac{1}{\sqrt{3}}\frac{|d_2|-|d_1|}{|d_3|}\right) \approx 13°$ for all wavelengths. The theoretical expectations ($d_{y,th}$) are reported together with the experimental results in **Table 1** for comparison.

For all three wavelengths, the "negative" orders have the opposite chirality to that of the "positive" orders. The measured distances ($d_{y,exp}$) and the circular dichroism (CD) calculated for the three wavelengths are reported in Table 1. The circular dichroism is calculated by CD = $100\% \cdot (S_{LCP} - S_{RCP})/(S_{LCP} + S_{RCP})$, where S_{LCP} and S_{RCP} are the PD maximum values measured with the LCP and RCP respectively. As can be seen from Table 1, the measured values of the circular dichroism of some orders of diffraction are very high and reach 70%. The experimental precision of the numerical values of CD, and of the positions of the diffraction orders, reported in Table 1, is determined and limited by the following factors: the possible sample inhomogeneity, the error during the spatial scan, and the mutual interaction of the signals coming from two neighboring

ADVANCED
SCIENCE NEWS

www.advancedsciencenews.com

ADVANCED
OPTICAL
MATERIALS

www.advopticalmat.de

Table 1. CD [%] values and positions $d_{y,exp}$ [mm] of the diffraction orders obtained from the experimental data in Figure 5, and the calculated values $d_{y,th}$ [mm] for a 2D hexagonal array with lattice period of 522 nm.

λ [nm]	Order no.	−3	−2	−1	+1	+2	+3
514	CD	+27	−22	−18	−	+70	−65
	$d_{y,exp}$	−2.20	−1.50	−0.65	+0.60	+1.75	+2.15
	$d_{y,th}$	−2.26	−1.59	−0.68	+0.68	+1.59	+2.26
496	CD	+45	−32	+13	−12	+38	−50
	$d_{y,exp}$	−2.00	−1.35	−0.60	+0.55	+1.60	+2.00
	$d_{y,th}$	−2.09	−1.46	−0.63	+0.63	+1.46	+2.09
458	CD	00	−15	−13	+20	−10	00
	$d_{y,exp}$	−1.70	−1.20	−0.50	−	+1.30	+1.70
	$d_{y,th}$	−1.78	−1.25	−0.54	+0.54	+1.25	+1.78

orders. The spatial scan of the "pump-probe" distance is performed with steps equal to 10 µm, with a ±0.1 µm precision. The level of interaction between two heat sources, which lie close to each other, is defined by the thermal diffusion length of the sample; in our case, this value is around 70 µm (at a modulation frequency of 36 Hz, thermal diffusivity 0.005 cm² s⁻¹), which is much lower compared to the minimum distance (500 µm) reported in Table 1. Analyzing all the mentioned contributions to the final measurement error, we estimate that the uncertainty of the values presented in Table 1 is less than 5%. The same argument will be valid for **Tables 2** and **3**, further in the manuscript.

Figure 5b,c show the polar plots of the PD signals as a function of quarter-wave plate rotation for diffracted orders +2 and +3 at 514 nm, and for orders −3 and +3 at 496 nm. To carry out these measurements, a preliminary scan was performed to identify the spatial positions of the diffracted orders. Then the probe beam is set where the maximum signal occurs for the selected order, and the signal is taken by rotating the quarter-wave plate from −180° to +180°. This is because when the probe beam is stopped on one of the modes and the quarter-wave plate is rotated, the measurements provide more reliable results for the chiral properties of each diffracted order.

Table 2. CD [%] and positions $d_{y,exp}$ [mm] of the diffraction orders obtained from the experimental data in Figure 6, and the calculated values $d_{y,th}$ [mm]. SR stands for the specularly reflected beam.

λ [nm]	Order no.	SR	+2	+3
514	CD	+4	+35	−5
	$d_{y,exp}$	−0.45	0.82	1.27
	$d_{y,th}$	−0.47	0.77	1.19
488	CD	00	−18	00
	$d_{y,exp}$	−0.46	0.70	1.13
	$d_{y,th}$	−0.47	0.70	1.11
476	CD	+4	0.0	+40
	$d_{y,exp}$	−0.47	0.66	1.10
	$d_{y,th}$	−0.47	0.66	1.10
458	CD	+6	−22	+38
	$d_{y,exp}$	−0.46	0.59	1.00
	$d_{y,th}$	−0.47	0.57	0.95

We further model this behavior in Lumerical. **Figure 6**a shows 3D maps of the six diffracted orders at 514 and 496 nm, for LCP and RCP excitations at normal incidence. The geometry of Ag-SNSA corresponds to that of Figure 4e, which has the additional in-plane tilt of the semishell and nanohole array. This tilt was estimated to be 20° in ref. [12], and we use this value here as well (see inset of Figure 1). As expected from the purely geometric treatment presented above, the diffracted orders spatially appear at the positions of a regular hexagon, which shrinks with the wavelength decrease. Further wavelength decrease would eventually lead to problems of order discrimination in PDT; namely, as the orders get closer to the center, they start to spatially overlap with neighboring orders and with the pump heat source. Fortunately, this can be solved by using a thicker substrate, which moves the orders to a longer $2L\tan(\theta_{ff})$. Further, chiral behavior corresponds to the one presented in Figure 4e, as Ag-SNSA is intrinsically chiral, and gives total absorption CD even at normal incidence; this agrees with our previous photoacoustic characterization of this sample in ref. [12]. In fact, the orders strongly differ for LCP and RCP excitations, and they are not spatially antisymmetric. Finally, we simulate the quarter-wave plate rotation influence on the intensity of modes +2 and +3, as they give the highest CD values, which invert the sign between the two orders. Figure 6b,c show good agreement with Figure 5b,c, respectively.

4.2. Oblique Incidence of the Pump Laser Beam

Next, we investigate the case in which the pump beam is incident onto the sample Ag-SNSA at the angle $\theta_{air}=20°$. First, we orient the metasurface so that the incident wave-vector projection onto the xy-plane coincides with the Ag-flux projection in the same plane ($\vec{n}$ and $\vec{k}$ lie in the same plane as in Figure 4a); then, we rotate the sample around the z-axis, as discussed in Section 4.1. (see the sketch of Figure 5a). We schematically show this approach in the inset of **Figure 7**a, where PDT results are shown at four different Ar wavelengths. The zeroth pump-probe distance again defines the central, pump-induced heat source. On the left ("negative" distances), we see the specularly reflected beam which exits at almost the same positions for all the wavelengths. This is expected, as its refraction in the glass medium does not depend on the coupling to the lattice; its only

**ADVANCED
SCIENCE NEWS**

www.advancedsciencenews.com

**ADVANCED
OPTICAL
MATERIALS**

www.advopticalmat.de

Table 3. Main features of the reconstructed temperature profile by using Equation (2) from PD data in Figure 5a, for excitation at 514 nm, presented as following; Column 1: diffraction order number; Column 2: circular dichroism (CD) calculated from the temperature peak; Columns 3,4: peak temperature for RCP and LCP respectively; Columns 5,6: percent absorbance of each diffraction order, calculated for an input pump beam power of 40 mW.

Order number	CD temp. [%]	Max temp. [°C]		Absorbance [%]	
		RCP	LCP	RCP	LCP
−3	17	0.25	0.35	1.2	1.8
−2	−16	0.22	0.16	1.2	0.8
−1	−11	0.98	0.78	2.7	2.1
0	00	11.5	11.5	16.0	16.0
+1	–	–	–	–	–
+2	59	0.38	1.47	1.0	4.0
+3	−64	0.45	0.10	2.0	0.5

dependence on the wavelength is through the dispersion of the glass refractive index, which is negligible in this wavelength range. This beam exhibits low CD, as reported in Table 2. On the other hand, for positive pump-probe distances, we monitor the orders +2 and +3. This is due to the fact that the oblique excitation brings the heat sources close to the center, which is also in agreement with Figure 4b,f. Again, the pump-probe distances increase with increasing wavelength, as expected because they depend on the coupling to the lattice. The beam intensities are different at all wavelengths, exhibiting sign and values which are governed by the metasurface's chirality. Specifically, at 458 nm we see that the chirality (CD) sign is switched between the two neighboring orders +2 and +3. Moreover, changing the wavelength a few tens of nm completely switches the CD sign, as it can be seen for the order +2 at 458 nm and at 514 nm. For this case, we further show the polar plot of the quarter-wave plate rotation, which is in qualitative agreement with numerical simulations (see Figure S2 in the Supporting Information). In Figure 7b, we show simulated 3D plots of the orders +2 and +3 at 458 nm (for clarity, the specularly reflected order SR is decreased 10 times in intensity). These two orders are the strongest in intensity, excluding SR, as previously

shown in Figure 4f; moreover, their chirality inverts as in the PD result. Next, we calculate numerical values of CD, applying the above formula with the intensities of each diffracted beam for LCP and RCP excitations. Figure S3 (Supporting Information) finally shows the good qualitative agreement of the simulated and experimental CD values. In Figure S4 (Supporting Information) we report on PD signals for Au-SNSA at 20° and at 514 nm; compared to Ag-SNSA behavior with the same excitation, we do not notice the important difference. We attribute the similar PD response to the higher influence of extrinsic chiral excitation (Figure 4f) with respect to the in-plane tilt existing only in Ag-SNSA. Finally, Figure S5 (Supporting Information) shows additional PD signal polar plots (quarter-wave plate rotation dependence) for Au-SNSA at 514 and 458 nm for the order +2; the opposite sign of CD for the two samples at 458 nm (-22% for Ag, see Table 2, end +12% for Au) might be due to highly material properties of metals at this wavelength.

Finally, the position of the orders +2 and +3 can be also calculated with geometrical considerations. For oblique incidence, theory predicts that each mth diffracted beam has its specific internal angle θ_m, and the real heat sources hexagon becomes
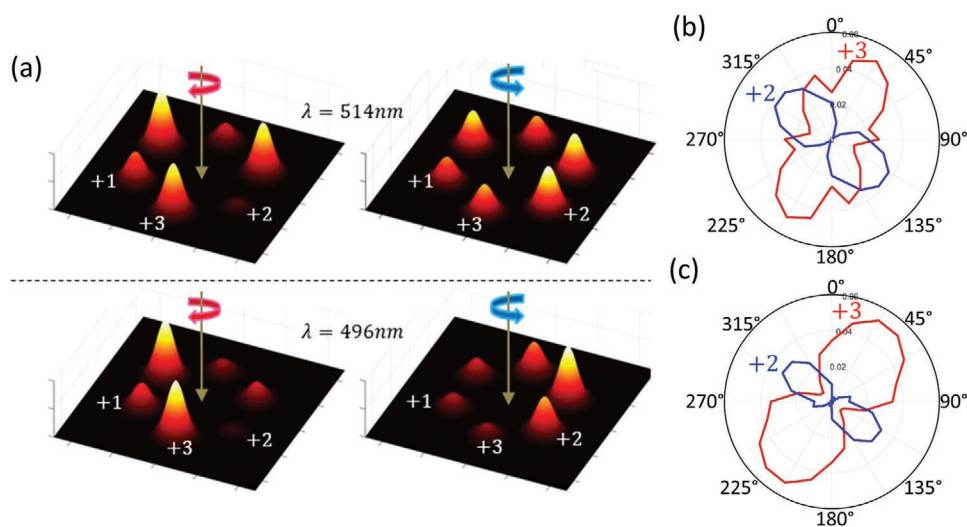

Figure 6. a) Simulated 3D plots for the normal incidence excitation at 514 nm (up) and at 496 nm (down), for LCP (blue) and RCP (red) excitation for Ag-SNSA. b,c) Polar plots of transmitted intensity as a function of quarter-wave plate rotation for the orders +2 and +3, at b) 514 nm, and c) 496 nm.
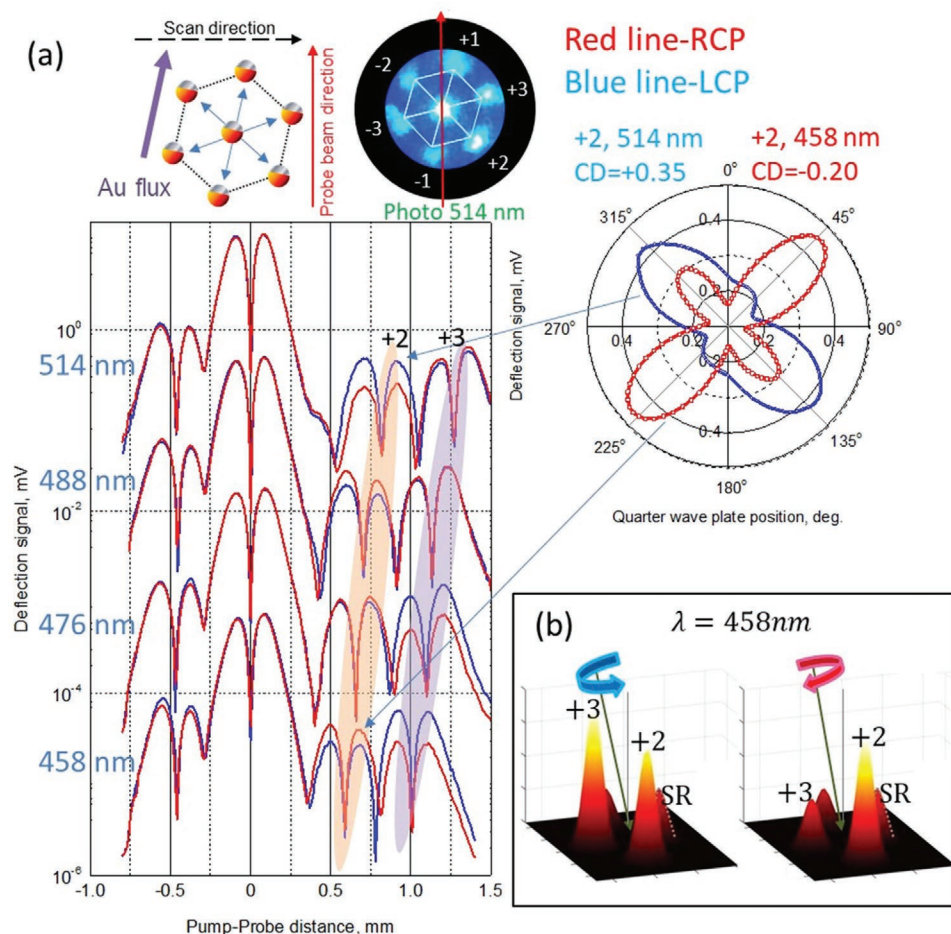
Figure 7. a) PD results (Log scale) for Ag-SNSA excited at 20° incidence along with the Ag flux (upper left schematic), at pump beam wavelengths 458 nm, 476 nm, 496, and 514 nm. The deflection signals are displayed as a function of circular polarization handedness (blue line: LCP, and red line: RCP), and the pump-probe distance. On the upper right, we show polar plots of the PD signal as a function of quarter-wave plate rotation for the order +2, with the pump beam at 514 nm (blue) and 458 nm (red). This small difference in wavelengths leads to a complete inversion of the chirality. b) Simulated 3D maps for the excitation at 458 nm and LCP (blue) and RCP (red) handedness, for the two orders reflected in the opposite part of the far-field with respect to the specular reflection SR (+2 and +3). The chirality is inverted in these two neighboring orders. For the sake of clarity, the intensity of the specular order SR is decreased 10 times.

irregular in the xy plane, with the position angle β_m of the vertices not equally spaced as in Section 4.1 (each $\pi/3$), and with irregular distances R_m from the center. The theoretical expectations are reported together with the experimental results in Table 2 for comparison.

4.3. Thermal Profile Reconstruction

A rough 1D map of the lateral heat flux induced by the pump incident and diffracted beams can be simply obtained by performing the probe beam scan as shown in Figures 5 and 7. Moreover, by analyzing both PD amplitude and phase signals in the proximity of each heat source (<0.3 mm), the effective thermal diffusion length and thermal diffusivity of the medium are calculated from the phase lag corresponding to the diffusion time delay between the heat source and the probe beam detection (i.e., phase method).[34,35] For each heat source we estimated an effective thermal diffusivity of about 0.005 cm² s⁻¹

(±10%), very close to the substrate diffusivity value (soda-lime glass).[34] This demonstrates that, at the modulation frequency of 36 Hz, the effective thermal diffusivity is not affected by the potentially higher thermally diffusive process at the submicron metasurface.

One important issue is to retrieve the metasurface temperature map from the PD scan signal (see Figure 5a). Previous works have already shown that, in the case of a heat source with cylindrical symmetry, Equation (1) can be inverted allowing to obtain the surface temperature rise from the following inverse integral:[40,41]

$$T(r) = -\frac{1}{\pi}\left(\frac{1}{n}\frac{dn}{dT}\right)^{-1}\int_{\infty}^{r}\frac{\Phi_\gamma(\gamma)}{\sqrt{\gamma^2 - r^2}}\,d\gamma \qquad (2)$$

where $\left(\frac{1}{n}\frac{dn}{dT}\right) \approx -10^{-6}\ °C^{-1}$, and r is the radial distance from the heat source (the extension to elliptical heat sources is also
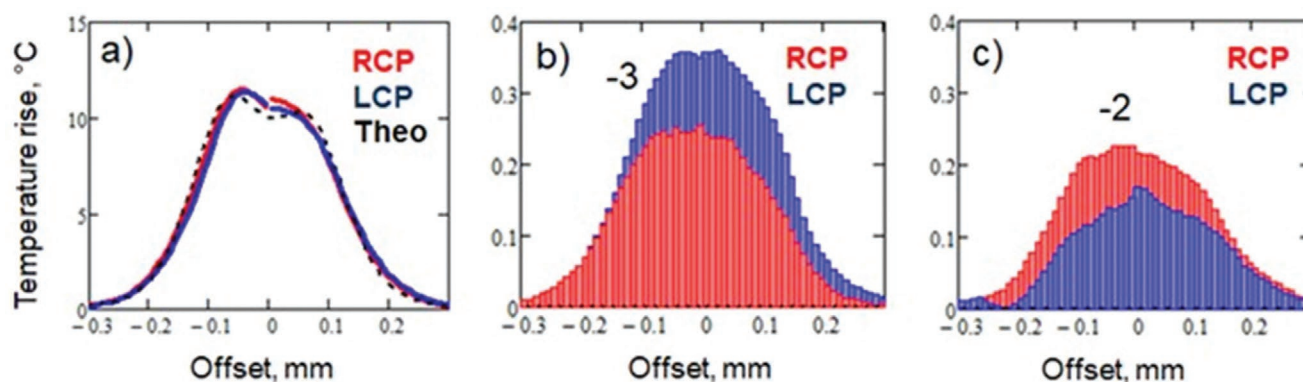
Figure 8. Temperature rise induced by the absorption of the diffracted beams and calculated by using Equation (2) from PD data in Figure 5a at 514 nm. The temperature profile is plotted for several diffracted beams: a) input pump beam; b) order -3; c) order -2; Dotted line is for the theoretical expectation. For all figures, the red and blue bars stand for RCP and LCP, respectively.

allowed). We have applied Equation (2) to process the PD data in Figure 4a, separately for each heat source within the spatial range of 0.3 mm. As an example, **Figure 8** shows the reconstructed surface temperature profile produced by the incident pump beam ($n = 0$) and by the diffracted beams with number $n = -3, -2$, for excitation at 514 nm. The temperature profiles exhibit Gaussian-like shapes. Chirality is clearly observed for $n \neq 0$. In particular, a change of the sign of chirality is also visible from $n = -3$ to $n = -2$.

The values of the maximum temperature rise and chirality have been reported in Table 3 for each analyzed heat source. Even though the sensibility of the transversal PDT is known to be very high,[33] in Table 3 we are limited to the second decimal place (10 mK); the reason is the mutual interaction of the signals arising from the two neighboring orders. Moreover, the reconstruction of the thermal profile through Equation (2) is affected by a truncation error of the integral, bringing an additional percentual uncertainty of 5% to the maximum temperature estimate for each order. Both the uncertainties are taken into account in Table 3.

The CD values calculated from the temperature peak (see column 2) are in agreement with the ones measured by PD amplitude (see Table 1). Finally, the values of absorbance are reported in Table 3. The absorbance is calculated as follows: from the temperature rise, one may calculate the thermal power of each source, and divide it by the initial input pump power of 40 mW. The absorbance is in fact the percent power ratio.

5. Conclusion

We have shown that the photodeflection technique can be used as a sensitive tool to study chiral effects in diffractive metasurfaces. We have investigated two samples obtained by nanosphere lithography and asymmetrically covered by Au or Ag. At the wavelengths of an Ar pump beam, these materials exhibit chirality-governed diffraction orders. Both extrinsic and intrinsic chiral effects are caught by placing the samples on a mirror, reflecting back the orders, and measuring deflection of the probe beam at positions of the thermal wave created due to absorption. The results are in good agreement with optical

numerical simulations and thermal analysis, which opens new perspectives on thermal control in metasurfaces. It is remarkable that PDT can reveal complex chiral behavior at the nanoscale. We believe that this approach can generally be used as a simpler alternative to diffraction spectroscopy. Moreover, combining it with chiral effects opens new perspectives for chiral sensing.

6. Experimental Section

Optical Simulations: In order to account for the hexagonal periodicity, and the dimensions of the PSN and metallic shells, the modeling procedure was employed from ref. [12]: a rectangular unit cell with dimensions a and $a\sqrt{3}$ is surrounded by Bloch boundary conditions (BBC) in x- and y-directions, and with perfectly matched layers in z-direction (a is the periodicity of the metasurface and it is equal to 522 nm for both samples). Two broadband plane-wave sources are combined to simulate general elliptical polarization; the sources are perpendicular to each other and differ in phase, while having other properties equal. The phase offset in the simulation corresponds to the QWP rotation angle in the experiment: 90° (−90°) models the QWP angle of 45° (−45°), which defines RCP (LCP) excitation.

Supporting Information

Supporting Information is available from the Wiley Online Library or from the author.

Acknowledgements

Conflict of Interest

The authors declare no conflict of interest.

Data Availability Statement

Research data are not shared.

2100670 (10 of 11)

[1] A. J. Hutt, S. C. Tan, *Drugs* **1996**, *52*, 1.

[2] L. A. Nguyen, H. He, C. Pham-Huy, *Adv. Nat. Sci.: Nanosci. Nanotechnol.* **2006**, *2*, 85.

[3] E. Tokunaga, T. Yamamoto, E. Ito, N. Shibata, *Sci. Rep.* **2018**, *8*, 17131.

[4] V. K. Valev, J. J. Baumberg, C. Sibilia, T. Verbiest, *Adv. Mater.* **2013**, *25*, 2517.

[5] M. Hentschel, M. Schäferling, X. Duan, H. Giessen, N. Liu, *Sci. Adv.* **2017**, *3*, e1602735.

[6] Y. Zhao, A. N. Askarpour, L. Sun, J. Shi, X. Li, A. Alù, *Nat. Commun.* **2017**, *8*, 14180.

[7] W. Liao, S. Liao, K. Chen, Y. Hsiao, S. Chang, H. Kuo, M. Shih, *Sci. Rep.* **2016**, *6*, 26578.

[8] S. Yang, X. Liu, H. Yang, A. Jin, S. Zhang, J. Li, C. Gu, *Adv. Opt. Mater.* **2020**, *8*, 1901448.

[9] A. Belardini, M. C. Larciprete, M. Centini, E. Fazio, C. Sibilia, *Phys. Rev. Lett.* **2011**, *107*, 257401.

[10] G. Leahu, E. Petronijevic, A. Belardini, M. Centini, C. Sibilia, T. Hakkarainen, E. Koivusalo, M. Rizzo Piton, S. Suomalainen, M. Guina, *Adv. Opt. Mater.* **2017**, *5*, 1601063.

[11] E. Petronijevic, M. Centini, A. Belardini, G. Leahu, T. Hakkarainen, C. Sibilia, *Opt. Express* **2017**, *25*, 14148.

[12] E. Petronijevic, G. Leahu, R. Li Voti, A. Belardini, C. Scian, N. Michieli, T. Cesca, G. Mattei, C. Sibilia, *Appl. Phys. Lett.* **2019**, *114*, 053101.

[13] T. Hakkarainen, E. Petronijevic, M. Rizzo Piton, C. Sibilia, *Sci. Rep.* **2019**, *9*, 5040.

[14] A. Belardini, G. Leahu, E. Petronijevic, T. Hakkarainen, E. Koivusalo, M. Rizzo Piton, S. Talmila, M. Guina, C. Sibilia, *Micromachines* **2020**, *11*, 225.

[15] E. Petronijevic, A. Belardini, G. Leahu, T. Hakkarainen, M. Rizzo Piton, E. Koivusalo, C. Sibilia, *Sci. Rep.* **2021**, *11*, 4316.

[16] C. Kuppe, C. Williams, J. You, J. T. Collins, S. N. Gordeev, T. D. Wilkinson, N. Panoiu, V. K. Valev, *Adv. Opt. Mater.* **2018**, *6*, 1800098.

[17] C. Kuppe, X. Zheng, C. Williams, A. W. A. Murphy, J. T. Collins, S. N. Gordeev, G. A. E. Vandenbosch, V. K. Valev, *Nanoscale Horiz.* **2019**, *4*, 1056.

[18] Z. Tao, J. Zhang, J. You, H. Hao, H. Ouyang, Q. Yan, S. Du, Z. Zhao, Q. Yang, X. Zheng, T. Jiang, *Nanophotonics* **2020**, *9*, 2945.

[19] E. Petronijevic, C. Sibilia, *Molecules* **2019**, *24*, 853.

[20] X. Zhao, M. H. Alizadeh, B. M. Reinhard, *ACS Photonics* **2017**, *4*, 2265.

[21] E. Petronijevic, E. M. Sandoval, M. Ramezani, C. L. Ordóñez-Romero, C. Noguez, F. A. Bovino, C. Sibilia, G. Pirruccio, *J. Phys. Chem. C* **2019**, *123*, 23620.

[22] G. Leahu, E. Petronijevic, A. Belardini, M. Centini, R. Li Voti, T. Hakkarainen, E. Koivusalo, M. Guina, C. Sibilia, *Sci. Rep.* **2017**, *7*, 2833.

[23] E. Petronijevic, G. Leahu, V. Mussi, C. Sibilia, F. A. Bovino, *AIP Adv.* **2017**, *7*, 025210.

[24] L. Goris, K. Haenen, M. Nesládek, P. Wagner, D. Vanderzande, L. De Schepper, J. D'Haen, L. Lutsen, J. V. Manca, *J. Mater. Sci.* **2005**, *40*, 1413.

[25] G. Leahu, R. Li Voti, C. Sibilia, M. Bertolotti, V. Golubev, D. A. Kurdyukov, *Opt. Quantum Electron.* **2007**, *39*, 305.

[26] S. Ilahi, F. Saidi, R. Hamila, N. Yacoubi, L. Auvray, H. Maaref, *Curr. Appl. Phys.* **2013**, *13*, 610.

[27] W. Dickmann, J. Dickmann, F. Feilong Bruns, S. Kroker, *J. Appl. Phys.* **2019**, *126*, 025106.

[28] D. A. Hanifi, N. D. Bronstein, B. A. Koscher, Z. Nett, J. K. Swabeck, K. Takano, A. M. Schwartzberg, L. Maserati, K. Vandewal, Y. van de Burgt, A. Salleo, A. P. Alivisatos, *Science* **2019**, *363*, 1199.

[29] H. Chima, N. Shiokawa, K. Seto, K. Takahashi, N. Hirosaki, T. Kobayashi, E. Tokunaga, *Appl. Sci.* **2020**, *10*, 1008.

[30] S. Morawiec, J. Holovský, M. J. Mendes, M. Müller, K. Ganzerová, A. Vetushka, M. Ledinský, F. Priolo, A. Fejfar, I. Crupi, *Sci. Rep.* **2016**, *6*, 22481.

[31] T. Cesca, N. Michieli, B. Kalinic, I. G. Balasa, R. Rangel-Rojo, J. A. Reyes Esqueda, G. Mattei, *Mater. Sci. Semicond. Process.* **2019**, *92*, 2.

[32] A. C. Boccara, D. Fournier, J. Badoz, *Appl. Phys. Lett.* **1980**, *47*, 130.

[33] W. B. Jackson, N. M. Amer, A. C. Boccara, D. Fournier, *Appl. Opt.* **1981**, *20*, 1333.

[34] M. Bertolotti, R. Li Voti, G. Leahu, C. Sibilia, *Rev. Sci. Instrum.* **1993**, *64*, 1576.

[35] M. Bertolotti, V. Dorogan, G. L. Liakhou, R. Li Voti, S. Paoloni, C. Sibilia, *Rev. Sci. Instrum.* **1997**, *68*, 1521.

[36] M. Bertolotti, G. L. Liakhou, R. Li Voti, S. Paoloni, C. Sibilia, *J. Appl. Phys.* **1998**, *83*, 966.

[37] Lumerical Solutions, Inc, http://www.lumerical.com/tcad-products/fdtd (accessed: April 2021).

[38] E. Petronijevic, A. Belardini, G. Leahu, T. Cesca, C. Scian, G. Mattei, C. Sibilia, *Appl. Sci.* **2020**, *10*, 1316.

[39] E. Petronijevic, H. Ali, N. Zaric, A. Belardini, G. Leahu, T. Cesca, G. Mattei, L. C. Andreani, C. Sibilia, *Opt. Quantum Electron.* **2020**, *52*, 176.

[40] M. Bertolotti, G. L. Liakhou, R. L.i Voti, C. Sibilia, *J. Therm. Anal.* **1996**, *47*, 51.

[41] M. Bertolotti, G. L. Liakhou, R. L.i Voti, R. P. Wang, C. Sibilia, A. V. Syrbu, V. P. Yakovlev, *Meas. Sci. Technol.* **1995**, *6*, 1278.